

Magnetic and Structural Studies of the Quasi-Two-Dimensional Spin-Gap System (CuCl)LaNb₂O₇

Makoto YOSHIDA*, Nobuyuki OGATA, Masashi TAKIGAWA†,
Jun-ichi YAMAURA, Masaki ICHIHARA, Taro KITANO¹,
Hiroshi KAGEYAMA¹, Yoshitami AJIRO¹, and Kazuyoshi YOSHIMURA¹

Institute for Solid State Physics, University of Tokyo, Kashiwa, Chiba 277-8581

¹*Department of Chemistry, Graduate School of Science, Kyoto University, Kyoto 606-8502*

(Received June 21, 2007; accepted July 27, 2007; published September 25, 2007)

We report magnetization, nuclear magnetic resonance (NMR), nuclear quadrupole resonance (NQR), and transmission electron microscopy (TEM) studies on the quasi-two-dimensional spin-gap system (CuCl)LaNb₂O₇, a possible candidate for the J_1 - J_2 model on a square lattice. A sharp single NQR line is observed at the Cu and Cl sites, indicating that both Cu and Cl atoms occupy a unique site. However, the electric field gradient tensors at the Cu, Cl, and La sites do not have axial symmetry. This is incompatible with the reported crystal structure. Thus the J_1 - J_2 model has to be modified. We propose alternative two-dimensional dimer models based on the NMR, NQR, and TEM results. The value of the hyperfine coupling constant at the Cu sites indicates that the spin density is mainly on the $d(3z^2 - r^2)$ orbital ($z \parallel c$). At 1.5 K, Cu- and Nb-NMR signals disappear above the critical field $B_{c1} \simeq 10.3$ T determined from the onset of the magnetization, indicating a field-induced magnetic phase transition at B_{c1} .

KEYWORDS: NMR, NQR, TEM, (CuCl)LaNb₂O₇, spin-gap, quantum spin system

DOI: [10.1143/JPSJ.76.104703](https://doi.org/10.1143/JPSJ.76.104703)

1. Introduction

Low-dimensional quantum spin systems with frustrating interactions have recently been studied intensively both from experimental and theoretical aspects. The $S = 1/2$ antiferromagnet on a square lattice with the nearest-neighbor and the next-nearest-neighbor interactions (the J_1 - J_2 model) is a well known example. When the nearest neighbor interaction J_1 is antiferromagnetic ($J_1 > 0$), the ground state has a Néel order with the wave vector (π, π) for $J_2/J_1 < 0.38$ while a collinear order with the wave vector $(\pi, 0)$ occurs for $J_2/J_1 > 0.52$.¹⁻³ A spin liquid phase is proposed between these phases near $J_2/J_1 \simeq 0.5$.¹⁻³ A spin liquid phase is also proposed for ferromagnetic J_1 ($J_1 < 0$) between the collinear phase for $J_2/J_1 < -0.51$ and the ferromagnetic phase for larger J_2/J_1 .³ The series of compounds (CuX)LaNb₂O₇ ($X = \text{Cl}, \text{Br}$) is a candidate for the J_1 - J_2 model with mixed ferro- and antiferromagnetic interactions.⁴⁻⁶ The structure is reported to be tetragonal (space group $P4/mmm$) with the CuX square lattice^{7,8} as shown in Fig. 1. In fact, (CuCl)LaNb₂O₇ has a singlet ground state with a spin-gap^{4,5} while (CuBr)LaNb₂O₇ shows a collinear antiferromagnetic order.⁶

In (CuCl)LaNb₂O₇, the spin-gap is estimated to be 27 K by fitting the susceptibility data to the isolated dimer model.⁴ The neutron inelastic scattering results also exhibit magnetic excitations with the gap of 2.3 meV, although the resolution is limited.⁴ On the other hand, the high-field magnetization measurements revealed a sudden increase at the critical field $B_{c1} = 10.3$ T.⁵ The Zeeman energy at B_{c1} , $g\mu_B B_{c1}/k_B = 15$ K, is apparently not sufficient to close the spin-gap at zero field. In addition, the magnetization saturates at $B_{c2} = 30.1$ T.⁵ The large interval between B_{c1} and B_{c2} indicates a large width of the triplet dispersion. This

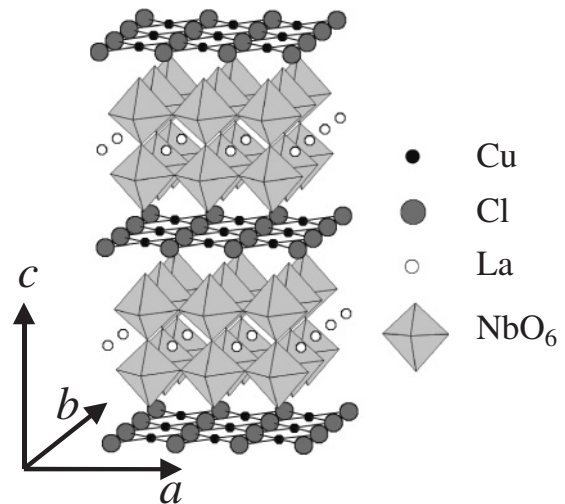


Fig. 1. Schematic drawing of the crystal structure of (CuCl)LaNb₂O₇.⁷⁾

is inconsistent with the neutron inelastic scattering data indicating that the triplet mode is almost dispersionless.⁴

There are also open issues about the crystal structure. The neutron diffraction study indicates that the Cl position deviates from the ideal $(0, 0, 1/2)$ position with the C_4 -symmetry in the tetragonal space group $P4/mmm$.⁸ If the structure deviates from the ideal square lattice, various ways to form a spin-gap become possible.⁹ Unambiguous determination of the structure is crucial for good understanding of a frustrated quantum spin system.

In this paper, we report magnetization, nuclear magnetic resonance (NMR), nuclear quadrupole resonance (NQR), and transmission electron microscopy (TEM) studies on (CuCl)LaNb₂O₇. Our results indicate that none of the Cu, Cl, and La sites has the C_4 -symmetry, incompatible with the reported tetragonal structure. Thus the J_1 - J_2 model for the simple square lattice has to be modified. We propose two-

*E-mail: yopida@issp.u-tokyo.ac.jp

†E-mail: masashi@issp.u-tokyo.ac.jp

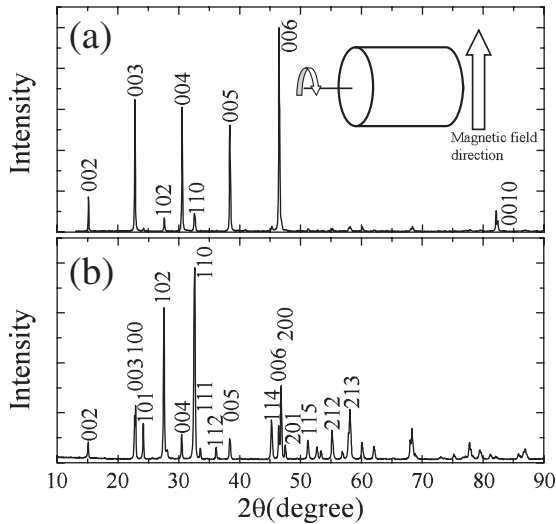


Fig. 2. X-ray diffraction patterns of the (a) aligned and (b) unaligned powder samples. The inset illustrates the method for preparing the aligned sample.

dimensional dimer models which are consistent with our NMR, NQR, and TEM results. Cu- and Nb-NMR signals disappear above the critical field $B_{c1} \simeq 10.3$ T at low temperatures, indicating a field-induced magnetic phase transition at B_{c1} .

2. Experiment

The powder sample of $(\text{CuCl})\text{LaNb}_2\text{O}_7$ was synthesized by the ion-exchange reaction of $\text{RbLaNb}_2\text{O}_7$ with CuCl_2 .^{4,7)} The magnetically aligned sample was prepared by rotating a cylindrical tube filled with the $(\text{CuCl})\text{LaNb}_2\text{O}_7$ powder and epoxy (STYCAST1266) in a magnetic field $B = 7$ T. The magnetic field was applied perpendicular to the rotating axis as shown in the inset of Fig. 2. In this configuration, the magnetic hard axis tends to align along the rotating axis. The X-ray diffraction pattern for the aligned sample was obtained with a MacScience M03X diffractometer using a monochromatic Cu $K\alpha$ radiation as shown in Fig. 2(a). Here the aligned axis was kept perpendicular to the scattering wave vector. Compared with the diffraction pattern for the unaligned powder shown in Fig. 2(b), the peaks corresponding to $(00n)$ planes are strongly enhanced in the aligned sample, where n is integer. This indicates that the c -axis is the magnetic hard axis. The rocking curve for these peaks with the half width of about 1.5° shows successful alignment. However, other peaks such as (102) or (110) are also observed in the aligned sample, indicating that a certain fraction of the sample remains unaligned.

The magnetic susceptibility χ was measured for the unaligned powder sample with a SQUID magnetometer (Quantum Design MPMS). NQR measurements in zero magnetic field have been performed for the ^{63}Cu and ^{35}Cl nuclei in the unaligned powder sample. Nuclear spin–lattice relaxation rates were measured by the inversion recovery method. NMR measurements in magnetic fields up to 11.7 T have been performed on the aligned sample with the magnetic field applied along the c -axis for $^{63,65}\text{Cu}$, $^{35,37}\text{Cl}$, ^{93}Nb , and ^{139}La nuclei. The TEM experiments were carried out at room temperature using a JEM2010F system with an

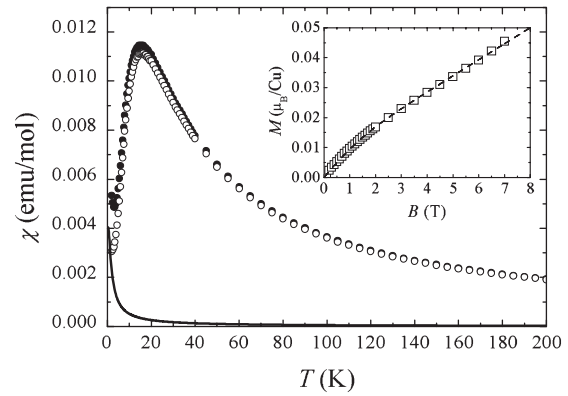


Fig. 3. Temperature dependence of χ measured for the unaligned powder sample at 1 T. The solid circles represent the raw data. The open circles represent χ after subtracting the impurity contribution shown by the solid line. The inset shows the magnetic field (B) dependence of the magnetization at 2 K. The dashed line is the fit to the form $M = NgS\mu_B B_S(x) + AB$.

operating voltage of 200 kV. The specimen was finely ground in methanol and then placed on a Cu microgrid mesh for TEM observation.

3. Results and Analysis

We first analyze the temperature dependence of χ in §3.1. In §3.2, we show the NQR results, which demonstrate that both Cu and Cl atoms occupy a unique site and there is no apparent disorder. The electric field gradient tensors at the Cu, Cl, and La sites are investigated from the field swept NMR spectra in §3.3. These results indicate deviation of the crystal structure from the reported one with a simple square lattice. In §3.4, the temperature dependences of the magnetic hyperfine shifts at the Cu and Cl sites are determined. Then the value of spin-gap is estimated. The hyperfine coupling constants are also determined at the Cu, Cl, and Nb sites. In §3.5, the high field behavior above B_{c1} is investigated at the Cu and Nb sites. Finally, we show the TEM result in order to provide additional information about the structure.

3.1 Magnetic susceptibility measurements

Figure 3 shows the temperature (T) dependence of χ measured at the field of 1 T. The peak at 16 K and rapid decrease at lower temperatures are quite consistent with the previous report,⁴⁾ indicating a singlet ground state. Below 4 K, however, χ increases with decreasing temperature probably due to magnetic impurities. In order to investigate the impurity contribution, we also measured magnetization M up to 7 T. The inset of Fig. 3 shows the B -dependence of M at 2 K. The data can be fitted by the sum of a term proportional to the Brillouin function $B_S(x)$ and a B -linear component $M = NgSB_S(x) + AB$ ($x = gS\mu_B B/k_B T$). A good agreement was obtained for the values $S = 1/2$, $N = 0.72\%/Cu$, and $N_A\mu_B A = 3.0 \times 10^{-3}$ emu/mol (N_A is the Avogadro constant) as shown by the dashed line in the inset of Fig. 3. The first term leads to the free spin contribution to χ , $N_A NgS\mu_B B_S(x)/B$, due to isolated magnetic impurities (the solid line in Fig. 3). By subtracting this term from the measured χ , we obtained the corrected χ shown by the open circles. The corrected χ maintains a finite value (3×10^{-3} emu/mol) as T goes to 0. It is also detected in the

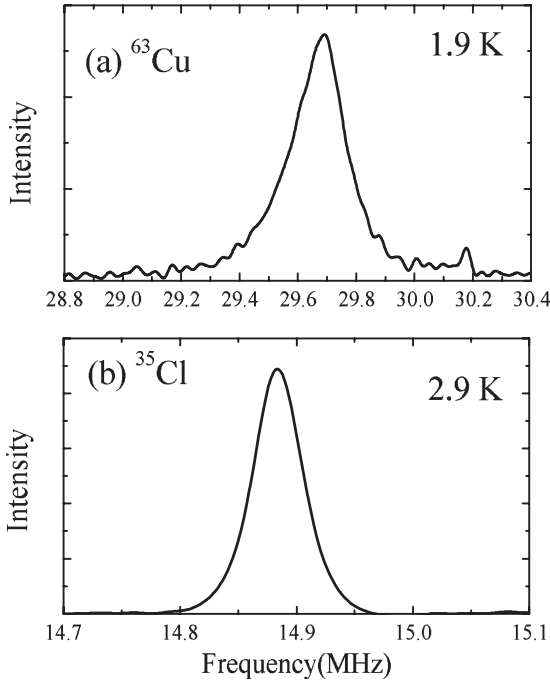


Fig. 4. NQR spectra (a) at the ^{63}Cu sites ($T = 1.9\text{ K}$) and (b) at the ^{35}Cl sites ($T = 2.9\text{ K}$).

magnetization curve as the B -linear component. This is much larger than the typical value of the Van Vleck susceptibility of Cu^{2+} (10^{-5} – 10^{-4} emu/mol). The NMR shifts at all sites do not show such large residual values at low temperatures as we discuss later. Hence the large residual susceptibility at low T is considered to be extrinsic, e.g. due to a secondary phase.

3.2 NQR spectra and relaxation rates

Figure 4 shows the NQR spectra at zero field for the ^{63}Cu and ^{35}Cl sites, both having the nuclear spin $I = 3/2$. A sharp single NQR line is observed for each nuclei. This shows that both Cu and Cl atoms occupy a unique site and there is no substantial disorder for the Cu and Cl positions. The NQR frequencies ν_{NQR} are determined to be 29.68 MHz for ^{63}Cu and 14.88 MHz for ^{35}Cl . The values of ν_{NQR} and the spectrum shape show no temperature dependence from 10 to 1.5 K, indicating that the structure is unchanged at low temperatures.

Figure 5 shows the inverse temperature dependence of $1/T_1$ at the ^{63}Cu and ^{35}Cl sites at zero field. At both sites, $1/T_1$ is well fitted by an activation law $1/T_1 \propto \exp(-E/k_B T)$. The activation energy is obtained as $E/k_B = 23 \pm 2\text{ K}$ for Cu and $E/k_B = 21 \pm 1\text{ K}$ for Cl. Below 4 K, $1/T_1$ deviates from the activation law and become independent of temperature below 3 K. The origin of the constant relaxation rate at low temperatures is likely to be impurities.

3.3 Field swept NMR spectra and EFG tensors

In the inset of Fig. 6, we show a typical field swept Cu-NMR spectrum for the aligned sample with the magnetic field B applied parallel to the c -axis. The spectrum has four sharp peaks assigned to the ^{63}Cu - and ^{65}Cu -NMR lines from the aligned part of the sample. The spectrum also shows a

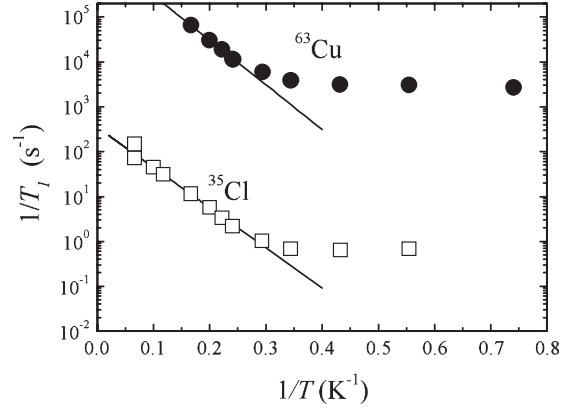


Fig. 5. Inverse temperature dependence of $1/T_1$ at the ^{63}Cu and ^{35}Cl sites. The solid lines show the fit to an activation law $1/T_1 \propto \exp(-E/k_B T)$.

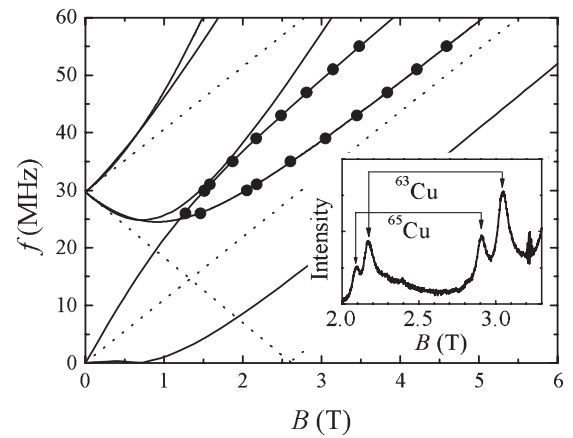


Fig. 6. Frequency–field diagram at 3 K at the ^{63}Cu sites in the applied magnetic fields B parallel to the c -axis. The dotted lines represent the resonance modes for the case of axially symmetric EFG around the c -axis. The solid lines are the fit to the results obtained from the Hamiltonian (2). The inset shows the Cu-NMR spectrum at 43 MHz.

broad tail spreading to higher field. This tail probably comes from the unaligned portion of the sample. The resonance fields are determined precisely from the peak positions. The frequency–field (f – B) diagram can be constructed by plotting the resonance fields for various NMR frequencies between 26 and 55 MHz as shown in Fig. 6.

The resonance frequency is generally determined from the following Hamiltonian including the magnetic hyperfine interaction and the electric quadrupole interaction,¹⁰⁾

$$H = -h\gamma(\mathbf{B} \cdot \mathbf{I} + \mathbf{I} \cdot \hat{\mathbf{K}} \cdot \mathbf{B}) + \frac{eQ}{6I(2I-1)} \sum_{\alpha,\beta} V_{\alpha\beta} \left[\frac{3}{2}(I_\alpha I_\beta + I_\beta I_\alpha) - \delta_{\alpha\beta} I^2 \right], \quad (1)$$

where h is the Planck's constant, Q is the nuclear quadrupole moment, γ is the gyromagnetic ratio, $\hat{\mathbf{K}}$ is the magnetic hyperfine shift tensor, $\delta_{\alpha\beta}$ is 0 ($\alpha \neq \beta$) or 1 ($\alpha = \beta$), and $V_{\alpha\beta} = \partial^2 V / \partial \alpha \partial \beta$ ($\alpha, \beta = x, y, \text{ or } z$) is the component of the electric field gradient (EFG) tensor. If the Cu sites have the C_4 -symmetry around the c -axis in the tetragonal crystal structure, $V_{\alpha\beta}$ is axially symmetric, that is, $V_{\alpha\beta} = 0$ for $\alpha \neq \beta$ and $V_{zz} = -2V_{xx}$ ($V_{xx} = V_{yy}, z \parallel c$). If the magnetic field is applied parallel to the symmetric c -axis, three resonance

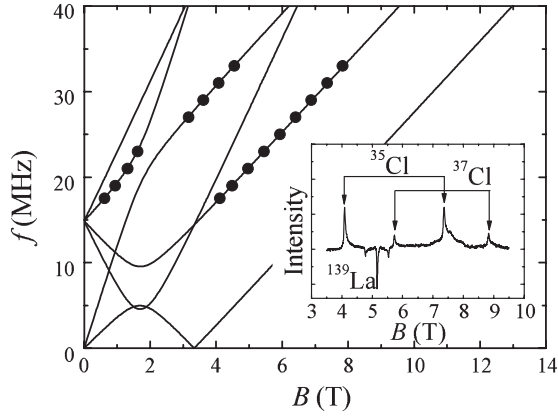


Fig. 7. Frequency–field diagram at 3 K at the ^{35}Cl sites in the applied magnetic fields B parallel to the c -axis. The solid lines show the fit obtained from the Hamiltonian (2). The inset shows the Cl-NMR spectrum at 31 MHz.

modes appear at the frequencies ν_R and $|\nu_{\text{NQR}} \pm \nu_R|$, where $\nu_R = (1 + K_{cc})\gamma B$ and $\nu_{\text{NQR}} = 3eQV_{zz}/2I(2I - 1)h$, provided that all the components of \hat{K} are much smaller than one. These results shown by the straight dotted lines in Fig. 6 are apparently in contradiction with the nonlinear behavior of the experimental data. This gives the direct evidence that the Cu sites do not have axial symmetry around the c -axis.

In the following, we assume that the c -axis is one of the principal axes of the EFG tensor at the Cu sites. This is the case, for example, when the Cu–Cl planes have the mirror symmetry. Although this assumption may not be strictly valid in the real structure, it is not possible to determine $V_{\alpha\beta}$ from the available data without any assumption. The nuclear Hamiltonian (1) is rewritten for the magnetic field parallel to the c -axis (z -axis) as

$$H = -h\gamma B(1 + K)I_z + \frac{h}{3}(\nu_x I_x^2 + \nu_y I_y^2 + \nu_z I_z^2), \quad (2)$$

where K is the magnetic hyperfine shift along the c -axis and $\nu_\alpha = [3eQ/2I(2I - 1)h]V_{\alpha\alpha}$.¹⁰ Although eq. (2) contains four parameters (ν_z , ν_x , ν_y , and K), the number of independent parameters can be reduced to two (K and ν_z) from the relations $\nu_x + \nu_y + \nu_z = 0$ and $\nu_{\text{NQR}} = \sqrt{\nu_z^2 + (\nu_x - \nu_y)^2}/3$, where the NQR frequency ν_{NQR} is determined to be 29.68 MHz in §3.1. Four eigenvalues of this Hamiltonian can be calculated analytically in the case of $I = 3/2$, resulting in six resonance modes. As shown in Fig. 6, the experimental data are well fitted by the solid lines obtained from eq. (2) with $\nu_z = 16.26 \pm 0.02$ MHz, $\nu_x = 13.37 \pm 0.02$ MHz, $\nu_y = -29.64 \pm 0.02$ MHz, and $K = 0.44 \pm 0.02\%$.

Figure 7 shows the f – B diagram at the ^{35}Cl sites obtained from the field swept NMR spectra of the aligned sample. A typical spectrum is shown in the inset of Fig. 7. The applied magnetic field B was parallel to the aligned direction (c -axis). The spectrum also shows the ^{139}La -NMR lines. The negative intensity is due to improper rf-pulse conditions, which were optimized for Cl signal. The f – B diagram can be fitted by solving the Hamiltonian (2) in the same way as has been done for the Cu sites. In Fig. 7, the solid lines show the results calculated for the parameter

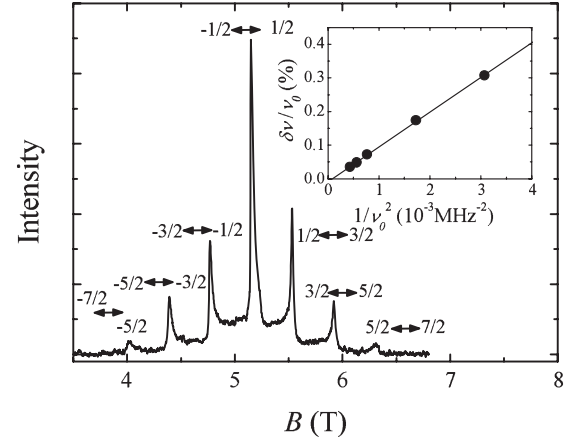


Fig. 8. Field swept NMR spectrum at the ^{139}La sites at 6 K and 31 MHz in the magnetic field parallel to the c -axis. The inset shows the $\delta\nu/\nu_0$ versus $1/\nu_0^2$ plot at 115 K.

values $\nu_z = 14.17 \pm 0.02$ MHz, $\nu_x = -3.13 \pm 0.02$ MHz, $\nu_y = -11.04 \pm 0.02$ MHz, and $K = 0.04 \pm 0.02\%$.

Figure 8 shows the field swept ^{139}La -NMR spectrum at 6 K and 31 MHz in the magnetic field parallel to the c -axis. The seven peaks split by the quadrupole interaction for $I = 7/2$ are clearly observed. Since the quadrupole interaction at the La sites is much smaller than that at the Cu and Cl sites, the second order perturbation theory is sufficient to extract the values of ν_α and K . We assume the c -axis to be one of the principal axes for EFG. The resonance frequency between the states $|m\rangle$ and $|m - 1\rangle$ is obtained from the Hamiltonian (2) as

$$\nu_{m \leftrightarrow m-1} = \nu_0(1 + K) - \left(m - \frac{1}{2}\right)\nu_z - \frac{(\nu_x - \nu_y)^2}{12\nu_0} \left[m(m-1) - \frac{19}{4} \right], \quad (3)$$

where $\nu_0 = \gamma B$.¹¹ If we define the frequency shift $\delta\nu_m \equiv \nu_{m \leftrightarrow m-1} - \nu_0$, the frequency shift of the central line $\delta\nu_{1/2}$ obeys the relation,

$$\frac{\delta\nu_{1/2}}{\nu_0} = K + \frac{5}{12} \frac{(\nu_x - \nu_y)^2}{\nu_0^2}. \quad (4)$$

Therefore, $\delta\nu_{1/2}/\nu_0$ plotted against $1/\nu_0^2$ should yield a straight line with the slope $(5/12)(\nu_x - \nu_y)^2$ and the intercept K at $1/\nu_0^2 = 0$. The inset of Fig. 8 shows the $\delta\nu/\nu_0$ versus $1/\nu_0^2$ plot at 115 K. We find that K at the La sites is almost zero ($-8 \times 10^{-3} \pm 2 \times 10^{-3}\%$) and $|\nu_x - \nu_y| = 1.57$ MHz. The value of ν_z is determined from the frequency shift for the satellite lines as $\nu_z = |\nu_{m \leftrightarrow m-1} - \nu_{-m+1 \leftrightarrow -m}|/(2m - 1)$. The values of ν_z , ν_x , and ν_y are determined to be 2.23 ± 0.02 , -0.33 ± 0.02 , and -1.90 ± 0.02 MHz, respectively.

The values of ν_α determined by NMR are listed in Table I for the Cu, Cl, and La sites. It should be noted that the values

Table I. Principal values of EFG tensors at the Cu, Cl, and La sites.

	Cu	Cl	La
ν_z (MHz)	16.26 ± 0.02	14.17 ± 0.02	2.23 ± 0.02
ν_x (MHz)	13.37 ± 0.02	-3.13 ± 0.02	-0.33 ± 0.02
ν_y (MHz)	-29.64 ± 0.02	-11.04 ± 0.02	-1.90 ± 0.02

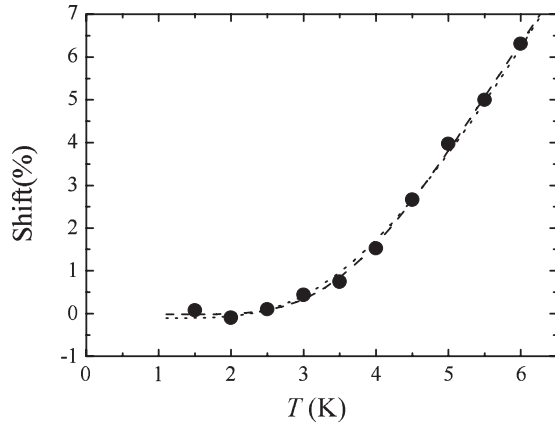


Fig. 9. Temperature dependence of K at the ^{63}Cu sites for the magnetic field parallel to the c -axis. The dashed and dotted lines show the calculated results for the isolated dimer model and the two dimensional coupled dimer model, respectively.

in Table I are determined on the assumption that the c -axis is one of the principal axes of EFG. The EFG tensor is not axially symmetric around the c -axis for all sites. That is, none of these sites has the C_4 -symmetry, which is incompatible with the reported tetragonal structure. Thus the J_1 - J_2 model for the simple square lattice has to be modified for proper description of this system. We discuss modified models in §4.3.

3.4 Hyperfine shift and coupling constant

By repeating the above analysis for different temperatures, we obtained the temperature dependence of K . Figure 9 shows the temperature dependence of K at the Cu sites in the magnetic field parallel to the c -axis. The shift consists of the contributions from the spin and Van Vleck susceptibility at the Cu sites, $K = K_s + K_{VV}$. Each term is related to the spin and the Van Vleck susceptibility as $K_s = (A_{hf}/N_A\mu_B)\chi_s$, $K_{VV} = (A_{orb}/N_A\mu_B)\chi_{VV}$. The chemical shift is expected to be negligibly small compared with the spin and orbital shifts due to d -electrons of Cu^{2+} . As shown in Fig. 9, K decreases with decreasing T and is extrapolated to zero at $T = 0$. This means K_s and A_{hf} are positive. Since K_{VV} is always positive, we can conclude that K_{VV} is nearly zero and K_s approaches zero at $T = 0$. It should be noted that while χ contains impurity contribution, K is free from impurities, and thus provides direct evidence for a spin-gap.

We estimate the spin-gap in two different models. The dashed line in Fig. 9 is the fit to the isolated dimer model

$$K = K_{VV} + \frac{C}{T} \left[1 + \frac{1}{3} \exp\left(\frac{E'}{k_B T}\right) \right]^{-1}, \quad (5)$$

from which we obtained $E'/k_B = 21.8 \text{ K}$ and $K_{VV} = -0.02 \pm 0.02\%$. Note that the shift was determined in the range of magnetic field from 1 to 5 T. Considering the reduction of the gap by the average field $g\mu_B(B)/k_B \simeq 4 \text{ K}$ ($\langle B \rangle = 3 \text{ T}$), the gap at zero field is estimated to be 26 K. This value is rather close to the gap ($\sim 27 \text{ K}$) estimated from the neutron inelastic scattering and the susceptibility measurements.^{4,5)} However, the isolated dimer model ignores the dispersion of the triplet excitations. In the opposite limit, where the triplets have large dispersion

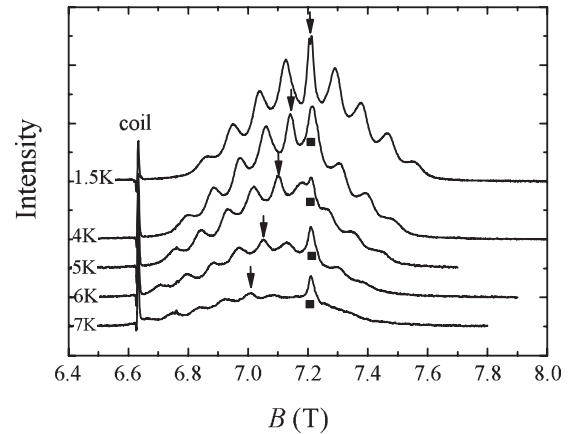


Fig. 10. Temperature dependence of the field swept spectrum at the Nb sites at 75 MHz for the applied magnetic fields B parallel to the c -axis.

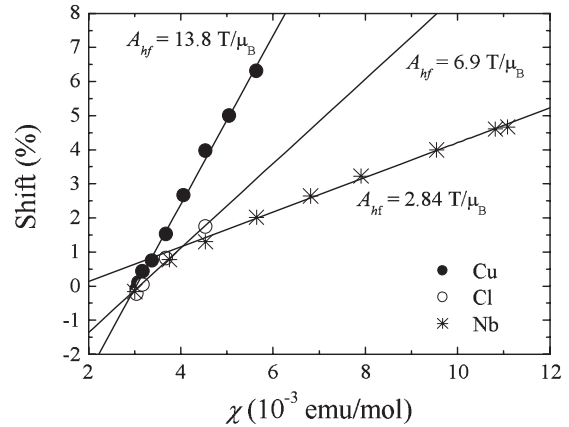


Fig. 11. K - χ plot for the Cu, Cl, and Nb sites.

$\epsilon_q = E'' + cq^2$, the spin susceptibility is determined by the excitation near the bottom of the dispersion $K_s \propto (1/T) \int D(\epsilon)n(\epsilon)d\epsilon \propto \exp(-E''/k_B T)$, where $D(\epsilon)$ is the density of state, which is constant for $\epsilon \geq E''$ in two dimension, and $n(\epsilon)$ is the Bose factor. The dotted line in Fig. 9 shows the fit to this model with $E''/k_B = 15 \text{ K}$. Therefore, the gap is estimated to be 19 K at zero field. The gap values obtained in this study are compared with the reported results in §4.1.

Figure 10 shows the temperature dependence of the field swept NMR spectrum at the Nb sites. The nine peaks for $I = 9/2$ is observed at 1.5 K and the central line is indicated by the arrow. The central and the eight satellite lines shift to lower fields with increasing temperature, indicating sizable hyperfine coupling at the Nb sites to spin magnetization of Cu ions. In addition, we observed another peak marked by the solid square in Fig. 10. This peak does not shift with temperature, indicating no hyperfine coupling to the Cu spins. In fact, $1/T_1$ for this peak is 10 times smaller than that for the intrinsic signal at low temperatures. Therefore, we conclude that this signal comes from extrinsic nonmagnetic phases. Imperfection of the ion-exchange reaction is a possible origin of such nonmagnetic impurely phases.

Figure 11 shows the K - χ plot for various sites obtained for the temperature range 1.5–20 K. Here, a Curie term due

Table II. Hyperfine coupling constants for $B \parallel c$.

	Cu	Cl	Nb
A_{hf} (T/ μ_B)	13.8 ± 0.3	6.9 ± 0.5	2.84 ± 0.08

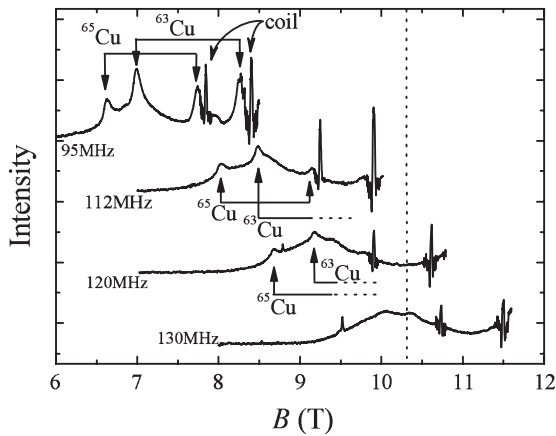


Fig. 12. Frequency dependence of the field swept NMR spectrum at the Cu sites at 1.5 K in the applied magnetic fields B parallel to the c -axis. The dotted lines show the critical field B_{c1} .

to magnetic impurities was removed from the χ data as described in §3.1. The hyperfine coupling constants A_{hf} for $B \parallel c$ are determined to be 13.8 ± 0.3 , 6.9 ± 0.5 , and 2.84 ± 0.08 T/ μ_B for the Cu, Cl, and Nb sites, respectively (Table II). Although the NMR shifts at all sites approach near zero as $T \rightarrow 0$, χ maintains a finite value (3×10^{-3} emu/mol) as mentioned in §3.1. Note that the impurity term from free spins has been already subtracted. The residual χ at low temperatures, which corresponds to the B -linear magnetization in the inset of Fig. 3, does not couple to any nuclei observed by NMR. Hence we conclude that it has as extrinsic origin.

3.5 High magnetic field region

Figure 12 shows the field swept NMR spectrum at 1.5 K for the Cu sites at different frequencies in the higher magnetic field region above $B_{c1} \simeq 10.3$ T. The very sharp peaks are due to the NMR-coil made from Cu. The $^{63,65}\text{Cu}$ -NMR lines from the aligned sample are indicated by the arrows. Their intensity decreases with increasing B and the peaks from the aligned sample disappear slightly below $B_{c1} = 10.3$ T. This is because the spin-spin relaxation time T_2 is getting shorter when the field approaches B_{c1} . There remains a broad signal near B_{c1} , observed in the spectrum at 130 MHz. Since this signal has much longer T_2 , it is probably due to some impurity phases.

Figure 13 shows the frequency dependence of the field swept spectrum at the Nb sites. The quadruple split peaks for ^{93}Nb ($I = 9/2$) are observed at 90 MHz. The intensity of the split peaks decreases with increasing B and the signal disappears slightly below B_{c1} in a similar way as has been observed for the Cu signals. Above B_{c1} , the spectrum with one central peak and broadened quadrupole satellites is observed (115 MHz). This signal probably has the same origin as the unshifted signal observed at 75 MHz at high temperatures (Fig. 10). In the inset of Fig. 13, the integrated

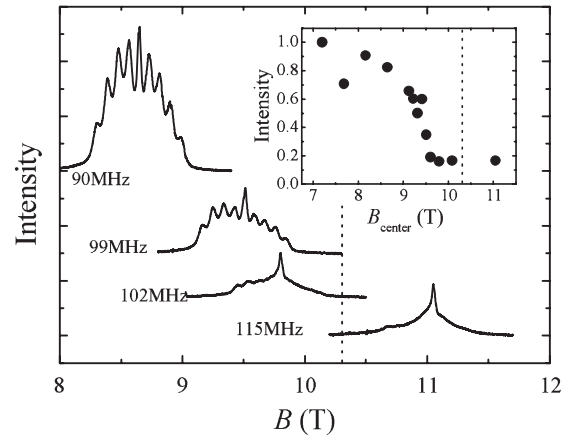


Fig. 13. Frequency dependence of the field swept NMR spectrum at the Nb sites at 1.5 K in the applied magnetic fields B parallel to the c -axis. The inset shows the B_{center} -dependence of the integrate intensity. The dotted lines show the critical field B_{c1} .

intensity of the whole spectrum is plotted against the field of the central line (B_{center}). The intensity normalized by the value at 7.2 T decreases with increasing B_{center} and vanishes at 9.5 T, slightly below B_{c1} , except for the contribution from impurity phases, indicating that a field-induced magnetic phase transition occurs around B_{c1} . The field-induced transition is also indicated by the recent specific heat measurements in magnetic fields.¹²⁾

3.6 TEM result

In order to obtain further information about the crystal structure, we performed TEM measurements at room temperature. Shown in Figs. 14(a) and 14(b) are the [001] zone lattice images that demonstrate contrasts with a special period of about 4 Å along $\langle 100 \rangle$, consistent with the

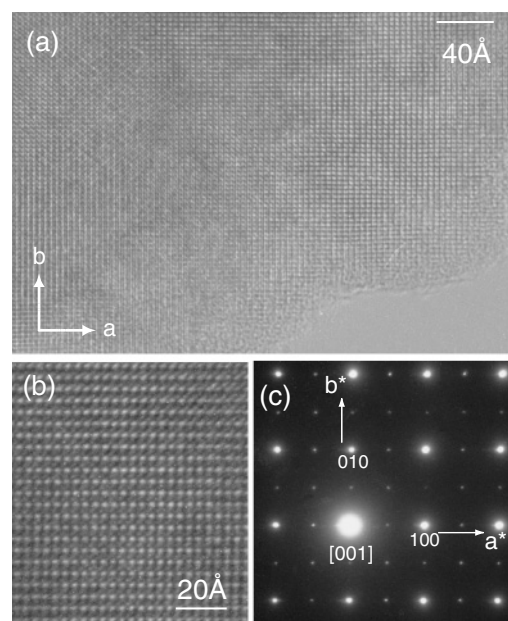


Fig. 14. (a) High-resolution TEM image of $(\text{CuCl})\text{LaNb}_2\text{O}_7$ at room temperature along the [001]-zone axis and (b) its enlarged view. (c) Corresponding electron diffraction pattern, where indices are given based on the tetragonal unit cell of the $P4/mmm$ structure.⁷⁾

lattice parameter. However, the corresponding electron diffraction [Fig. 14(c)] has revealed weak reflections such as $(1/2, 0, 0)$ or $(0, 1/2, 0)$, in addition to strong fundamental reflections relevant to the reported crystal structure. The weak reflections are commensurate and indicate the doubling of the lattice period of both a - and b -axes, i.e., the size of the unit cell is given by $2a \times 2b$. Such a superstructure has not been detected even by high q -resolution synchrotron X-ray diffraction,¹³ presumably due to tiny modulation of the atoms and/or small domain size. Note that the superstructure reflection at $(1/2, 1/2, 0)$ was observed in $(\text{FeCl})\text{LaNb}_2\text{O}_7$.¹³

4. Discussion

4.1 Spin-gap

The gap value in $(\text{CuCl})\text{LaNb}_2\text{O}_7$ is still controversial, while it has been investigated by several experimental methods. The most direct method is the inelastic neutron scattering, which shows the magnetic excitation with the gap energy of 2.3 meV (26.7 K).⁴ Although it is possible that the limited energy resolution masks fine structure of the neutron spectrum and the true gap may be somewhat smaller, the large discrepancy between this value and the gap derived from the critical magnetic field, $g\mu_B B_{c1}/k_B = 15$ K, cannot be explained by such an effect.

From the susceptibility measurements, the gap is estimated to be 27 K by using the isolated dimer model.⁴ The magnetic hyperfine shift determined by NMR is free from impurity contribution and provides more reliable spin susceptibility. Using the isolated dimer model, the gap value is determined to be 26 K, consistent with the susceptibility results. We have also examined a two-dimensional coupled dimer model with a large width of the triplet dispersion and obtained the gap value of 19 K. Since these two models correspond to the opposite limits of zero and infinite width of the dispersion, the values 26 and 19 K set the upper and the lower bounds for the true gap. From the NQR relaxation rate $1/T_1$ at the Cu and Cl sites, the gap value is determined to be 23 ± 2 and 21 ± 1 K, respectively, consistent with the above range. This range is still significantly larger than $g\mu_B B_{c1}/k_B (= 15$ K).

To reconcile the discrepancy between the gap estimated at low magnetic fields and B_{c1} , Kageyama *et al.* proposed formation of two-triplet bound states with $S = 2$.⁵ If two-triplet bound states are stabilized due to frustration, the gap can close before B reaches $\Delta/g\mu_B$ and a nematic order may be realized above B_{c1} .¹⁴ The Cu- and Nb-NMR signals were undetectable above B_{c1} at 1.5 K due to divergence of $1/T_2$ as mentioned before (Figs. 12 and 13). To investigate the magnetic structure above B_{c1} , we need measurements at higher fields and lower temperatures.

4.2 d -orbital

The experimental determination of A_{hf} and K_{VV} at the Cu sites provides information about the Cu d -orbital. In this section, we compare the experimental results of A_{hf} and K_{VV} with the calculated values. Figure 15 shows the orbital energy levels for Cu^{2+} in tetragonal crystal fields. The Cu^{2+} ions have one d -hole with either $d(x^2 - y^2)$ or $d(3z^2 - r^2)$ wave function. The hyperfine coupling constants $A_{\parallel}^{\text{hf}}$ (for $B \parallel z$) and A_{\perp}^{hf} (for $B \perp z$) are expressed as

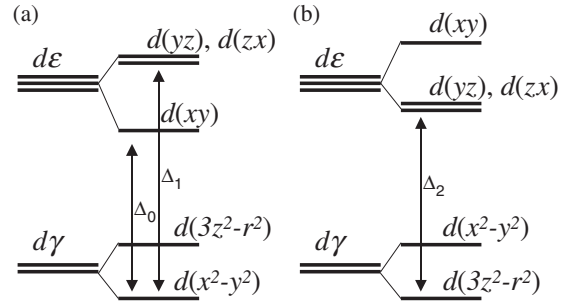


Fig. 15. Orbital energy levels for Cu^{2+} in a tetragonal crystal field. The ground state wave function is $d(x^2 - y^2)$ in (a) or $d(3z^2 - r^2)$ in (b).

$$\begin{aligned}
 A_{\parallel}^{\text{hf}} &= \frac{\mu_0 \mu_B}{4\pi} \langle r^{-3} \rangle \left(-\kappa - \frac{4}{7} + \frac{6}{7} \frac{\lambda}{\Delta_1} - \frac{8\lambda}{\Delta_0} \right) \\
 A_{\perp}^{\text{hf}} &= \frac{\mu_0 \mu_B}{4\pi} \langle r^{-3} \rangle \left(-\kappa + \frac{2}{7} + \frac{11}{7} \frac{\lambda}{\Delta_1} \right) \text{ for } d(x^2 - y^2) \\
 A_{\parallel}^{\text{hf}} &= \frac{\mu_0 \mu_B}{4\pi} \langle r^{-3} \rangle \left(-\kappa + \frac{4}{7} + \frac{6}{7} \frac{\lambda}{\Delta_2} \right) \\
 A_{\perp}^{\text{hf}} &= \frac{\mu_0 \mu_B}{4\pi} \langle r^{-3} \rangle \left(-\kappa - \frac{2}{7} - \frac{45}{7} \frac{\lambda}{\Delta_2} \right) \text{ for } d(3z^2 - r^2),
 \end{aligned} \tag{6}$$

where μ_0 is the permeability of vacuum, κ is the core polarization coefficient, λ is the spin-orbit coupling parameter, and Δ_i ($i = 0, 1, 2$) is the energy between the ground state and the excited state shown in Fig. 15.^{15,16} The values of κ , λ , and $\langle r^{-3} \rangle$ for Cu^{2+} ions are common to all insulating materials within 10–20%, typically given as $\kappa = 0.28$, $\lambda = -8.8 \times 10^{-2}$ eV, and $\langle r^{-3} \rangle = 4.26 \times 10^{31} \text{ m}^{-3}$.^{15,16} Δ_i depends on materials but should be of the order of a few eV. We take $\Delta_i = 2.0$ eV.^{15,16} By using these values, $A_{\parallel}^{\text{hf}}$ and A_{\perp}^{hf} are estimated to be -24.1 and $2.71 \text{ T}/\mu_B$ for $d(x^2 - y^2)$ and 10.2 and $-12.2 \text{ T}/\mu_B$ for $d(3z^2 - r^2)$, respectively. Compared with the experimental values, $A_{\text{hf}} (= 13.8 \text{ T}/\mu_B)$, $A_{\parallel}^{\text{hf}}$ for $d(x^2 - y^2)$ and A_{\perp}^{hf} for $d(3z^2 - r^2)$ can be excluded because they lead to large negative shifts. Note that the magnetic field is parallel to the c -axis in the experiment, and we consider the cases where the z -axis of the orbital is either parallel or perpendicular to the c -axis. Among the other two cases, $A_{\parallel}^{\text{hf}}$ for $d(3z^2 - r^2)$ is by far the favorable.

The vanishing Van Vleck susceptibility $K_{\text{VV}} \simeq 0$ for $B \parallel c$ also supports the $d(3z^2 - r^2)$ orbital. For $B \parallel z$, the Van Vleck susceptibility χ_{VV} (emu/mol) is calculated as

$$\chi_{\text{VV}} = N_A \mu_B^2 \sum_{n \neq 0} \frac{|\langle \psi_n | L_z | \psi_0 \rangle|^2}{\epsilon_n - \epsilon_0}, \tag{7}$$

where ψ_0 is the grand state with the energy ϵ_0 and ψ_n is the excited state with the energy ϵ_n . For the $d(3z^2 - r^2)$ orbital, χ_{VV} is zero. On the other hand, χ_{VV} for $d(x^2 - y^2)$ is calculated to be $N_A \mu_B^2 / \Delta_1 \simeq 1.6 \times 10^{-5}$ emu/mol, leading to $K_{\text{VV}} = 2 \langle r^{-3} \rangle \chi_{\text{VV}} / N_A = 0.23\%$. This is clearly incompatible with the experimental observation. Therefore, we conclude that the Cu spins are on the d -orbital consisting mainly of $d(3z^2 - r^2)$. This is natural because the Cu–O bonding (1.84 Å) is much shorter than the Cu–Cl bonding in the ab plane (3.14 or 2.40 Å).⁸ Such structure and the difference of the ionic valence (O^{2-} vs Cl^-) make the

$d(3z^2 - r^2)$ orbital favorable for the d -hole. It should be noted that broken axial symmetry revealed by our NMR data should allow slight mixing of other components such as $d(x^2 - y^2)$. The large hyperfine field at the Nb sites can then be understood as due to the transferred hyperfine interaction through the $d(3z^2 - r^2)$ orbital. We suspect that the inter-plane exchange interaction through the path Cu–O–Nb–O–Nb–O–Cu and the nearest-neighbor exchange interaction through the path Cu–O–O–Cu may not be completely negligible.

4.3 Possible model

Precise structural information of the CuCl plane is crucial to understand the origin of the spin-gap in this compound. Our NQR results show that both Cu and Cl have only one site and there is no apparent disorder. This means that periodic superstructure should be realized, even though the domain size of the superstructure may be very small. Although Caruntu *et al.* proposed disorder in the Cl position based on their neutron diffraction experiments,⁸⁾ their results are not necessarily incompatible with the NQR results because possibility of a superstructure was not considered in the analysis of the neutron data. In addition to the NQR results, the EFG tensor does not have axial symmetry at the Cu, Cl, and La sites and the TEM result shows that the unit cell is doubled along both the a - and the b -axes from the original square lattice. Therefore, J_1 – J_2 model for the simple square lattice has to be modified. Whangbo and Dai proposed models of ring clusters with even number of spins based on the neutron results to account for the spin-gap. They lead, however, to several inequivalent Cu and Cl sites, inconsistent with our NQR results.

The rather large spin-gap suggests that the real structure has such a feature that allows natural formation of Cu dimers. Figures 16(a), 16(b), 16(e), and 16(f) show examples of such structures, where we assume that Cu maintains the ideal position for the square lattice $(1/2, 1/2, 1/2)$. The structure in Fig. 16(a) is simplest and leads to a two-dimensional dimer system as shown in Fig. 16(c). Here, dimers are formed by the dominant exchange path J_1 , and connected with each other by J'_1 , J''_1 , and J_2 . If J_1 is antiferromagnetic, a spin-gap is naturally formed. This structure has only one Cu and Cl site. The neutron diffraction study suggests that Cl moves off the ideal $(0, 0, 1/2)$ position to one of the $(x, 0, 1/2)$, $(-x, 0, 1/2)$, $(0, x, 1/2)$, and $(0, -x, 1/2)$ positions in a random manner.⁸⁾ The structure in (a) is an ordered version of the structure proposed from the neutron experiments.⁸⁾ However, the unit vectors $\hat{a} \pm \hat{b}$ of the structure (a) leads to the superstructure reflection at $(1/2, 1/2, 0)$ but cannot account for the observed TEM reflections such as $(1/2, 0, 0)$ and $(0, 1/2, 0)$. Therefore, Cl should take more general positions. We propose three models (b), (e), and (f), which are consistent with both the NQR and TEM results. In the structure (b), Cl moves off the ideal $(0, 0, 1/2)$ position to a position, $(x, y, 1/2)$, $(-x, y, 1/2)$, $(x, -y, 1/2)$, or $(-x, -y, 1/2)$, still maintaining only one site. The dominant exchange path J_1 makes the dimers, which are connected by other exchange paths J'_1 , J''_1 , J_2 , and J'_2 as shown in Fig. 16(d). In the structures (e) and (f), Cl moves off to $(x, 0, 1/2 + \delta)$, $(x, 0, 1/2 - \delta)$, $(-x, 0, 1/2 + \delta)$, or $(-x, 0, 1/2 - \delta)$. The

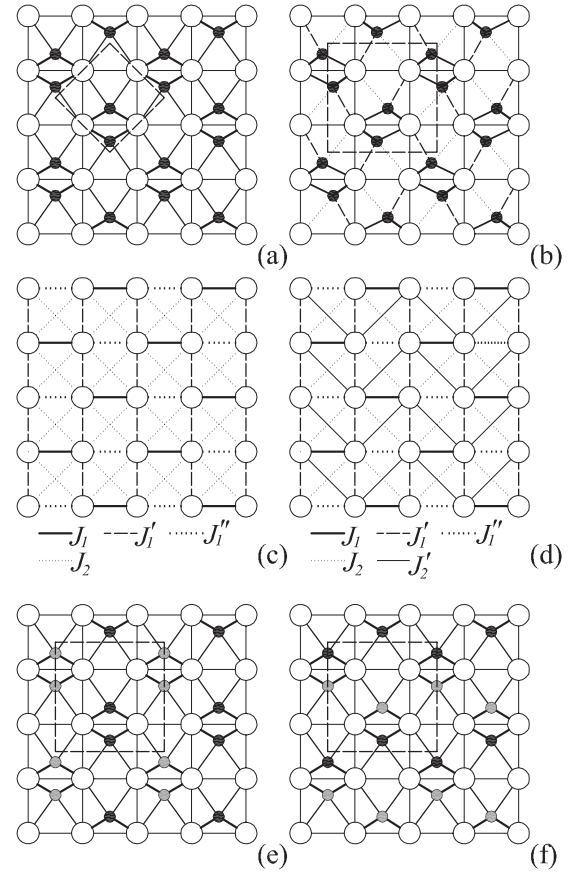


Fig. 16. Possible structures for the CuCl plane. The open and solid circles represent the Cu and Cl ions, respectively. The dashed lines in (a), (b), (e), and (f) indicate the unit cell for the superstructure. In the structure (e) and (f), the solid and gray spheres represent the Cl atoms above and below the Cu plane, respectively.

solid and gray spheres represent the Cl atoms above and below the Cu plane, respectively. In both (e) and (f), the exchange paths are the same as the structure (a) that is shown in Fig. 16(c). Both models (c) and (d) generate frustration.

A useful insight is obtained by comparing the magnetic ground state of $(\text{CuCl})\text{LaNb}_2\text{O}_7$ and $(\text{CuBr})\text{LaNb}_2\text{O}_7$, which shows a collinear antiferromagnetic order.⁶⁾ We have observed a large internal field of 16 T at the $^{79,81}\text{Br}$ sites in $(\text{CuBr})\text{LaNb}_2\text{O}_7$ by zero field NMR. The details will be published in a separate paper. If J_1 is antiferromagnetic in $(\text{CuBr})\text{LaNb}_2\text{O}_7$, the internal field at the Br sites should be canceled out for the structures (a), (e), and (f). Therefore, if the two materials have the same structure, (b) is the only possibility. However, the exchange interaction through Cl or Br is very sensitive to small structural variation and often changes from ferromagnetic to antiferromagnetic.¹⁷⁾ Therefore, J_1 for $(\text{CuBr})\text{LaNb}_2\text{O}_7$ may be ferromagnetic, even if J_1 for $(\text{CuCl})\text{LaNb}_2\text{O}_7$ is antiferromagnetic. If J_1 is ferromagnetic in the structures (a), (e), and (f), a large internal field of the ordered moment survives. Therefore, both models (c) and (d) are possible. It seems that these examples exhaust possible structures within the condition of the uniqueness of the Cu and Cl sites and the doubled periodicity along the a - and b -axes, although we are not able to prove rigorously.

5. Summary

NMR, NQR, and TEM results of $(\text{CuCl})\text{LaNb}_2\text{O}_7$ have been reported. A sharp single NQR line observed at each Cu and Cl site indicates that both Cu and Cl atoms occupy a unique site. The electric field gradient tensor shows that there is no axial symmetry around the c -axis at the Cu, Cl, and La sites. These results indicate that the J_1 – J_2 model for the simple square lattice has to be modified. We propose a two-dimensional dimer model for this compound. Cu- and Nb-NMR signals disappear above the critical field $B_{c1} \simeq 10\text{T}$ at low temperatures, indicating a field-induced magnetic phase transition occurs at B_{c1} .

Acknowledgment

We would like to thank T. Momoi, N. Shannon, H. Nojiri, and K.-Y. Choi for valuable discussions. This work was supported by Grants-in-Aid for Scientific Research (Nos. 18740202 and 17684018) and Grants-in-Aid on Priority Areas “Invention of Anomalous Quantum Materials” (Nos. 16076204 and 16076210) from the Ministry of Education, Culture, Sports, Science and Technology of Japan.

- 1) G. Misguich and C. Lhuillier: in *Frustrated Spin Systems*, ed. H. T. Diep (World Scientific, Singapore, 2003); cond-mat/0310405.
- 2) N. Read and S. Sachdev: *Phys. Rev. Lett.* **62** (1989) 1694.

- 3) N. Shannon, B. Schmidt, K. Penc, and P. Thalmeier: *Eur. Phys. J. B* **38** (2004) 599.
- 4) H. Kageyama, T. Kitano, N. Oba, M. Nishi, S. Nagai, K. Hirota, L. Viciu, J. B. Wiley, J. Yasuda, Y. Baba, Y. Ajiro, and K. Yoshimura: *J. Phys. Soc. Jpn.* **74** (2005) 1702.
- 5) H. Kageyama, J. Yasuda, T. Kitano, K. Totsuka, Y. Narumi, M. Hagiwara, K. Kindo, Y. Baba, N. Oba, Y. Ajiro, and K. Yoshimura: *J. Phys. Soc. Jpn.* **74** (2005) 3155.
- 6) N. Oba, H. Kageyama, T. Kitano, J. Yasuda, Y. Baba, M. Nishi, K. Hirota, Y. Narumi, M. Hagiwara, K. Kindo, T. Saito, Y. Ajiro, and K. Yoshimura: *J. Phys. Soc. Jpn.* **75** (2006) 113601.
- 7) T. A. Kodenkandath, J. N. Lalena, W. L. Zhou, E. E. Carpenter, C. Sangregorio, A. U. Falster, W. B. Simmons, C. J. O'Connor, and J. B. Wiley: *J. Am. Chem. Soc.* **121** (1999) 10743.
- 8) G. Caruntu, T. A. Kodenkandath, and J. B. Wiley: *Mater. Res. Bull.* **37** (2002) 593.
- 9) M.-H. Whangbo and D. Dai: *Inorg. Chem.* **45** (2006) 6227.
- 10) C. P. Slichter: *Principles of Magnetic Resonance* (Springer-Verlag, Berlin, Heidelberg, 1990).
- 11) G. H. Stauss: *J. Chem. Phys.* **40** (1964) 1988.
- 12) A. Kitada, Z. Hiroi, Y. Tsujimoto, T. Kitano, H. Kageyama, Y. Ajiro, and K. Yoshimura: *J. Phys. Soc. Jpn.* **76** (2007) 093706.
- 13) N. Oba, H. Kageyama, T. Saito, M. Azuma, W. Paulus, T. Kitano, Y. Ajiro, and K. Yoshimura: *J. Magn. Magn. Mater.* **310** (2007) 1337.
- 14) N. Shannon, T. Momoi, and P. Sindzingre: *Phys. Rev. Lett.* **96** (2006) 027213.
- 15) A. Abragam and B. Bleaney: *Electron Paramagnetic Resonance of Transition Ions* (Oxford Univ. Press, New York, 1980).
- 16) C. H. Pennington, D. J. Durand, C. P. Slichter, J. P. Rice, E. D. Bukowski, and D. M. Ginsberg: *Phys. Rev. B* **39** (1989) 2902.
- 17) Y. Inagaki, A. Kobayashi, T. Asano, T. Sakon, H. Kitagawa, M. Motokawa, and Y. Ajiro: *J. Phys. Soc. Jpn.* **74** (2005) 2683.